

Estimating flow parameter distributions using ground-penetrating radar and hydrological measurements during transient flow in the vadose zone

Michael B. Kowalsky^{a,*}, Stefan Finsterle^b, Yoram Rubin^a

^a Civil and Environmental Engineering, 435 Davis Hall, University of California, Berkeley, CA 94720-1710, USA

^b Earth Sciences Division, Lawrence Berkeley National Laboratory, 1 Cyclotron Road, MS 90-1116, Berkeley, CA 94720, USA

Received 25 August 2003; received in revised form 10 March 2004; accepted 11 March 2004

Available online 17 April 2004

Abstract

Methods for estimating the parameter distributions necessary for modeling fluid flow and contaminant transport in the shallow subsurface are in great demand. Soil properties such as permeability, porosity, and water retention are typically estimated through the inversion of hydrological data (e.g., measurements of capillary pressure and water saturation). However, ill-posedness and non-uniqueness commonly arise in such non-linear inverse problems making their solutions elusive. Incorporating additional types of data, such as from geophysical methods, may greatly improve the success of inverse modeling. In particular, ground-penetrating radar (GPR) methods have proven sensitive to subsurface fluid flow processes and appear promising for such applications. In the present work, an inverse technique is presented which allows for the estimation of flow parameter distributions and the prediction of flow phenomena using GPR and hydrological measurements collected during a transient flow experiment. Specifically, concepts from the pilot point method were implemented in a maximum a posteriori (MAP) framework to allow for the generation of permeability distributions that are conditional to permeability point measurements, that maintain specified patterns of spatial correlation, and that are consistent with geophysical and hydrological data. The current implementation of the approach allows for additional flow parameters to be estimated concurrently if they are assumed uniform and uncorrelated with the permeability distribution. (The method itself allows for heterogeneity in these parameters to be considered, and it allows for parameters of the petrophysical and semivariogram models to be estimated as well.) Through a synthetic example, performance of the method is evaluated under various conditions, and some conclusions are made regarding the joint use of transient GPR and hydrological measurements in estimating fluid flow parameters in the vadose zone.

© 2004 Published by Elsevier Ltd.

Keywords: Vadose zone; GPR; Pilot point; Joint inversion; Transient data; Hydraulic parameters

1. Introduction

Predicting flow phenomena, such as the time a spilled contaminant takes to migrate through the vadose zone and into an aquifer, or predicting soil moisture profiles for agriculture management applications, requires characterization of soil properties such as permeability, porosity, and water retention. Existing techniques allow point values of these parameters to be measured in situ or

in the laboratory (using soil cores). However, fluid flow parameters are commonly heterogeneous, and uncertainty in their spatial distributions makes it difficult to model fluid flow and contaminant transport using point measurements alone. Furthermore, point measurements are commonly limited due to their collection being expensive, time consuming and invasive (creating the potential for preferential flow paths). Alternative techniques that allow for the inference of flow parameter distributions are therefore in high demand.

Sequential simulation techniques may be used to generate parameter fields that reflect specified patterns of spatial correlation and preserve point measurements [14,20,42,43]. However, the generation of fields that accurately predict flow given hydrological data and

* Corresponding author. Present address: Earth Sciences Division, Lawrence Berkeley National Laboratory, 1 Cyclotron Road, MS 90-1116, Berkeley, CA 94720, USA.

E-mail addresses: mbkowalsky@lbl.gov (M.B. Kowalsky), sfinsterle@lbl.gov (S. Finsterle), rubin@ce.berkeley.edu (Y. Rubin).

point measurements typically requires the employment of inverse methods. While substantial progress has been made in accounting for multi-dimensional spatial heterogeneity in the saturated zone, methods for the vadose zone are less common and have been mostly limited to one-dimensional cases, usually uniform or layered soil columns [11,24,28,35,47,54]. In addition to the problems of ill-posedness and non-uniqueness, endemic to all types of groundwater inverse problems [7], the non-linearity introduced through saturation-dependent flow parameters undoubtedly contributes to the relative shortage of inverse techniques for variably saturated media [42,45].

As groundwater inverse problems can be made more amenable to solution by incorporating additional types of data [34], integrating geophysical measurements into inverse methods for the vadose zone is a particularly promising area of research, though still in its infancy [4,25]. Proving increasingly useful for monitoring moisture profiles in the vadose zone are geophysical methods such as ground-penetrating radar (GPR) [1,5,15,21,22,26,51] and electrical resistance tomography (ERT) [53]. Applications are rare in which geophysical methods are used quantitatively in the actual estimation of flow parameters in the vadose zone. Some progress has been made in this direction, such as in the work of Binley et al. [4], who investigated the use of ERT and crosshole GPR, collected during a tracer injection test, to estimate by trial and error the effective value of saturated hydraulic conductivity.

In the present work, we describe a method that allows for estimation of flow parameter distributions in the vadose zone jointly using hydrological and geophysical measurements collected during a transient flow experiment. We consider the special case in which permeability is the only non-uniform flow parameter and its log value may be treated as a space random function (SRF) characterized by a lognormal distribution with known patterns of spatial correlation (i.e., known semivariograms). Through a maximum a posteriori (MAP) inversion framework that employs concepts from the pilot point method, the log permeability distribution and additional flow parameters may be estimated. The employed methodology allows for the generation of multiple parameter distributions that reproduce point measurements, contain the specified patterns of spatial correlation, and are consistent with the hydrological and geophysical measurements. The resulting parameter distributions can be used for hydrological modeling and also to calculate parameter probability density functions (pdfs), which provide a measure of parameter uncertainty.

While additional data types such as capillary pressure and flow rate could easily be included in the method we describe, the measurements considered in this study include only point values of permeability, profiles of water saturation at boreholes (available through methods such

as neutron probe logging), and crosshole GPR data (e.g., travel times or GPR-derived estimates of water saturation, as is described below).

The requirements for modeling flow in variably saturated media are described next, as are the GPR measurements used in the current study. Following that is a description of the proposed inversion methodology and its implementation, and then a synthetic example which allows for (1) evaluation of the method's performance under various conditions, (2) consideration of experimental designs, and (3) conclusions to be drawn regarding the joint use of GPR and hydrological measurements for flow inversion.

2. Modeling flow in the vadose zone

Modeling flow phenomena in the vadose zone requires a forward model that relates fluid flow parameters, such as porosity and permeability, to observational data, such as measurements of water saturation and pressure. For the case of incompressible flow of water in non-deformable porous media, variably saturated flow can be modeled with the Richards' equation, which is given by

$$\phi \frac{\partial S_w}{\partial t} + \nabla \cdot \left[\frac{K(S_w)}{\rho_w g} \nabla P^c(S_w) - K(S_w) \hat{\mathbf{z}} \right] = 0, \quad (1)$$

where K and P^c , both functions of water saturation S_w , are the hydraulic conductivity and the capillary pressure, respectively, ρ_w is the water density, g is the gravitational constant, ϕ is the porosity, and $\hat{\mathbf{z}}$ is the vertically oriented unit vector, positive upward [2]. The hydraulic conductivity is defined as

$$K = k \frac{k_{\text{rel}}(S_w) \rho_w g}{\mu_w}, \quad (2)$$

where k is the permeability (or absolute permeability), k_{rel} is the dimensionless relative permeability (the only component of K that is a function of water saturation), and μ_w is the dynamic viscosity of water.

Solving (1) and (2) additionally requires functions that cast the relative permeability and capillary pressure in terms of water saturation. A common parametric formulation for this purpose is given by van Genuchten [50] as:

$$k_{\text{rel}} = \sqrt{S} \left[1 - \left(1 - S^{m-1} \right)^m \right]^2, \quad (3)$$

$$P^c = -\alpha^{-1} \left(S^{m-1} - 1 \right)^{1-m}, \quad (4)$$

$$S = \frac{S_w - S_w^{\text{res}}}{S_w^{\text{sat}} - S_w^{\text{res}}}, \quad (5)$$

where k_{rel} and P^c are the relative permeability and capillary pressure functions, respectively, m (dimensionless)

and α (e.g., in units of Pa^{-1}) are soil-specific parameters, S is the normalized water saturation, and S_w^{res} and S_w^{sat} are the soil-specific residual and maximal water saturation values, respectively. In the current work, the variably saturated flow simulator TOUGH2 [39] is used to simulate transient flow experiments. Details of the flow simulator are omitted here for brevity but are well documented in Pruess [39].

Assuming that the relative permeability and capillary pressure functions described above are valid, the spatial distributions of the following variables must be characterized in order to model flow in the vadose zone: k , ϕ , α , m , S_w^{res} and S_w^{sat} . While a number of studies show that spatial variability of these parameters can be significant [27,44], data relevant for modeling applications are limited. In the present work, the only parameter considered spatially variable is k .

Observational data which may allow for estimation of the parameters mentioned above include hydrological data (e.g., measurements of water saturation) and geophysical data, such as from GPR methods (described next).

3. Ground-penetrating radar measurements

Since GPR methods allow for the collection of non-invasive high resolution data that are sensitive to fluid saturation, they are potentially useful for parameter estimation methods in the vadose zone. However, it should be noted that GPR methods perform best in sites lacking highly electrically conductive materials, such as clay-rich soils [13]. GPR wave attributes such as the electromagnetic (EM) wave velocity and attenuation are governed by electrical parameters including the electrical conductivity and the dielectric constant, both of which depend on water saturation [12]. For common earth materials [13], the EM wave velocity is related to the dielectric constant through the simple relationship

$$v \approx \frac{c}{\sqrt{\kappa}}, \quad (6)$$

where c is the EM wave velocity in free space and κ is the effective dielectric constant, which can be related to water saturation with a petrophysical model [41,48]. The model used by Roth et al. [41], also known as the CRIM model, gives the effective dielectric constant as

$$\kappa = [(1 - \phi)\sqrt{\kappa_s} + S_w\phi\sqrt{\kappa_w} + (1 - S_w)\phi\sqrt{\kappa_a}]^2, \quad (7)$$

where κ_s , κ_w , and κ_a are the dielectric constants for the solid, water, and air components of the soil, respectively, ϕ is the soil porosity, and S_w is the water saturation. It should be noted that potential measurement errors of these parameters (particularly the component dielectric constants) lead to significant uncertainty in estimated effective dielectric constant values (or, as in an applica-

tion of this model that is described below, to uncertainty in estimated water saturation values).

In crosshole GPR applications, high-frequency EM pulses (commonly with central frequencies of 100 or 250 MHz) are propagated between boreholes in various antenna configurations [12]. For multiple offset gather (MOG) surveys, measurements are recorded at an array of receiver positions for each of multiple transmitter positions. MOG data sets allow for two- (or three-) dimensional reconstruction of GPR wave attributes, most commonly EM wave velocity or attenuation. However, collecting such data sets can be time and labor intensive, limitations particularly relevant in dynamic flow situations. For the current study, we focus instead on the configuration that is more quickly and easily collected, the zero-offset profile (ZOP), in which only measurements at successive depths are collected (i.e., while the antennas in their respective boreholes are kept at equal depths). It is assumed that the water saturation profile does not change significantly in the time it takes to conduct a ZOP survey.

A GPR wave attribute that is potentially sensitive to the distribution of water saturation is the arrival time. For demonstration, a synthetic ZOP data set was generated for a model with spatially variable water saturation (techniques for simulating GPR are discussed below). The arrival times, picked at the point in time when the waveform amplitude departs from zero, are indicated in Fig. 1a and are also plotted in Fig. 1b. As an alternative to using ZOP travel times directly as observational data for flow inversion, they may also be converted to EM wave velocity and then to average water saturation provided a suitable petrophysical model exists. For example, the combination of (6) and (7) gives the GPR-inferred average water saturation at a given depth as

$$S_{w,\text{GPR}} = \frac{TcL^{-1} - (1 - \phi)\sqrt{\kappa_s} - \phi\sqrt{\kappa_a}}{\phi(\sqrt{\kappa_w} - \sqrt{\kappa_a})}, \quad (8)$$

where T is the recorded travel time, and L is the separation distance between boreholes. Through (8), the travel times recorded in a ZOP survey (e.g., Fig. 1b) can be converted to a depth profile of horizontally averaged inter-borehole water saturation (Fig. 1c) provided that soil porosity can be estimated.

The vertical resolution of ZOP profiles depends on the electrical parameters of the soil and on the GPR antenna frequency [12]. For a source frequency of 250 MHz, a resolution of ~ 10 cm is typically achieved (corresponding to the quarter wavelength of the propagating wave traveling at 0.1 m/ns), whereas, a resolution closer to 25 cm is expected for a source frequency of 100 MHz. It should be noted that there is a tradeoff between increases in resolution gained using higher frequency antennas and the resulting decreases in signal penetration [13,49].

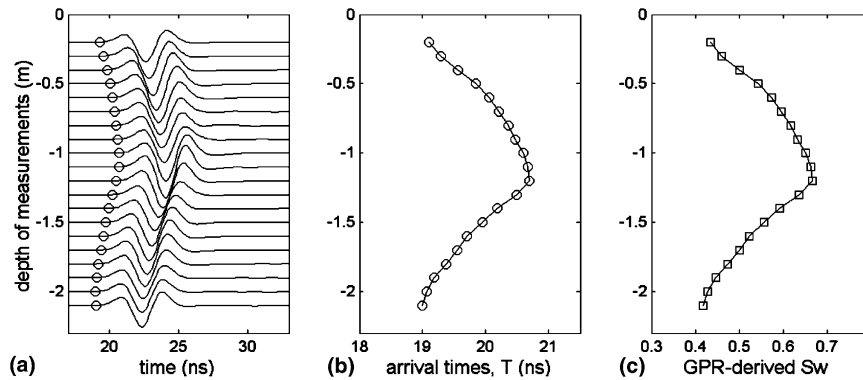


Fig. 1. (a) Simulated GPR waveforms in ZOP configuration (one waveform simulated for each transmitting/receiving antenna depth) with picked arrival times indicated by circles, (b) distribution of arrival times T with depth, and (c) estimates of inter-borehole water saturation derived from arrival times T (using Eq. (8)), assuming that porosity and antenna separation distance are known.

The application of GPR methods to groundwater inverse problems requires a forward model that relates soil properties, such as water saturation and porosity, to observational data. Numerous techniques are available for simulating GPR wave propagation, ranging from ray based [6], to pseudo-spectral [8], to time domain finite difference methods [31]. Ideally, GPR data that may be modeled include travel times (such as in Fig. 1b) or water saturation profiles (such as in Fig. 1c) estimated through application of (8). In the synthetic example presented below, for simplicity we calculate average inter-borehole water saturation values directly and use these as “pseudo-GPR” measurements (i.e., the arithmetic mean of the simulated water saturation values between borehole antenna positions is taken with an averaging thickness proportional to the GPR antenna frequency). This approximation is justified by considering the high degree of similarity between water saturation profiles obtained in this way and the water saturation profiles inferred using a GPR time domain finite difference method (shown below).

4. Methodology for parameter estimation

In developing an approach for estimating flow parameter distributions using hydrological and geophysical measurements jointly, concepts from the pilot point method [9,33] are implemented within a Bayesian, maximum a posteriori (MAP) framework. Before describing details of the inverse methodology employed in the present work, some key concepts from the pilot point method are first summarized.

4.1. Pilot point concepts

Application of pilot point methods commonly involves the generation of a spatially correlated parameter field, and subsequent perturbation of the field at select

locations, called pilot points, in order to allow for an improved match between measured and simulated observational data (e.g., piezometric head measurements). The parameter field is perturbed in such a way as to maintain known patterns of spatial correlation and parameter point measurements (if available). The goal is then to identify the optimal perturbation at each pilot point location through inversion of observational data using an appropriate optimization algorithm (i.e., the goal is to modify the initial random field in such a way as to allow for the best possible fit between measured and simulated observational data). For a given initial random field realization (i.e., with a fixed seed number), a single parameter field is obtained through inversion. Repeating this procedure for multiple random field realizations (i.e., each with a different seed number) yields multiple parameter fields, each of which is conditional to point measurements, contains the specified spatial correlation patterns, and is consistent with observational data. Parameter pdfs may then be calculated, giving mean values and corresponding uncertainty measures. Of perhaps even greater use are the obtained parameter fields that may be used for hydrological modeling (e.g., to predict flow phenomena and to quantify prediction uncertainty).

Details in previous implementations of the pilot point method differ greatly, including on how pilot point locations are chosen, how perturbations are propagated, which observational data are used, and details regarding the weighting of parameters, observational data, and prior information in the objective function (discussed below). Some of the perceived benefit of early work on the pilot point method derived from its flexibility in choosing pilot point locations. Later innovative work involved finding more systematic and efficient approaches for positioning pilot points. RamaRao et al. [40] proposed a method for adding pilot points sequentially, after finding their optimal locations with adjoint sensitivity analyses. However, concerns were

later raised regarding the addition of pilot points sequentially [10]. In an alternate implementation given by Gomez-Hernandez et al. [19], pilot points were placed on a pseudo-regular grid (and called master points), and inversion for their values was performed simultaneously. They found optimal master point spacing to be on the order of 2 to 3 points per correlation length. (Note that although the method we describe in the next section has similarities with the implementation of Gomez-Hernandez et al. [19], we will refer to the unknowns as pilot points rather than master points.)

Much of the previous work employing pilot point concepts involved horizontal flow in the saturated zone, where the parameter of interest was the log transmissivity, and observational data included steady state and transient piezometric head measurements [9,19,32,40]. Wen et al. [52] extended the implementation developed by Gomez-Hernandez et al. [19] to include transient tracer data and found in a synthetic study that the combination of piezometric head and tracer data allowed for improvements in transport prediction.

Of interest in the present work is to apply a version of the pilot point method to a vadose zone problem, and to include geophysical, in addition to hydrological measurements, as observational data. Such an approach is desirable as it lacks restrictions common to other approaches which include linearizations of the flow equation and assumptions of stationarity of the dependent variables (which is particularly problematic near boundaries and is in fact quite restrictive in the vadose zone) [53]. However, a potential limitation to pilot point methods lies in the significant computational demands arising for large problems (many forward calculations are required to evaluate pilot point perturbations, and multiple inversions must be performed for different random field realizations). These concerns are less restrictive with increasing computing speed and availability of parallel computing.

4.2. Pilot point concepts in MAP framework

For the present study we consider a domain in the unsaturated zone that is undergoing transient flow and is characterized by a spatially variable log permeability $Y(\mathbf{x})$, which is assumed to be a SRF with known patterns of spatial correlation (e.g., the possibly anisotropic semivariogram model is known from outcrop studies). The remaining flow parameters are assumed to be spatially uniform and uncorrelated with $Y(\mathbf{x})$. The goal of the inversion is to estimate $Y(\mathbf{x})$ and additional flow parameters given:

1. *Hydrological measurements*, in this case assumed to be local water saturation measurements, are defined as $\mathbf{z}_H = S_w[(\mathbf{x}, \mathbf{t})_H] + \mathbf{v}_H$, taken over the intervals and at measurement times $(\mathbf{x}, \mathbf{t})_H = (\mathbf{x}_{H,i}, t_{H,i})_{i=1,\dots,M_H}$,

$(\mathbf{x}_{H,i}, t_{H,i})_{i=1,\dots,M_H}, \dots, (\mathbf{x}_{H,i}, t_{H,N_H})_{i=1,\dots,M_H}$, where the M_H measurement locations are \mathbf{x}_H , and the N_H measurement times are \mathbf{t}_H , and \mathbf{v}_H is the measurement error (of length $M_H \times N_H$) associated with measurement of \mathbf{z}_H ;

2. *GPR measurements* (presently the horizontally averaged water saturation values inferred from ZOP surveys), defined as $\mathbf{z}_{\text{GPR}} = S_{w,\text{GPR}}[(\mathbf{x}_{\text{Tx}}^*, \mathbf{x}_{\text{Rx}}^*, \mathbf{t}_{\text{GPR}})] + \mathbf{v}_{\text{GPR}}$, are taken over the intervals and at times $(\mathbf{x}_{\text{Tx}}^*, \mathbf{x}_{\text{Rx}}^*, \mathbf{t}_{\text{GPR}}) = (\mathbf{x}_{\text{Tx},i}, \mathbf{x}_{\text{Rx},i}, t_{\text{GPR},i})_{i=1,\dots,M_{\text{GPR}}}, (\mathbf{x}_{\text{Tx},i}, \mathbf{x}_{\text{Rx},i}, t_{\text{GPR},2})_{i=1,\dots,M_{\text{GPR}}}, \dots, (\mathbf{x}_{\text{Tx},i}, \mathbf{x}_{\text{Rx},i}, t_{\text{GPR},N_{\text{GPR}}})_{i=1,\dots,M_{\text{GPR}}}$, where the M_{GPR} transmitting and receiving antenna positions are \mathbf{x}_{Tx} and \mathbf{x}_{Rx} , respectively, the N_{GPR} measurement times are \mathbf{t}_{GPR} , and \mathbf{v}_{GPR} is the measurement error (of length $M_{\text{GPR}} \times N_{\text{GPR}}$) associated with estimates of $S_{w,\text{GPR}}$; and,
3. *Log permeability point measurements* $\mathbf{Y}_{\text{meas}} = Y(\mathbf{x}_{\text{meas}})$, collected at the M_Y locations given by \mathbf{x}_{meas} and assumed to be error free and from a support scale equal to or greater than that at which flow is modeled.

In the synthetic example below, the hydrological and GPR measurements are collected at the same times making $N_H = N_{\text{GPR}} = N$, and $\mathbf{t}_H = \mathbf{t}_{\text{GPR}} = \mathbf{t}$.

In the spirit of the pilot point method, $Y(\mathbf{x})$ is a function of the M_{pp} pilot points \mathbf{Y}_{pp} at locations \mathbf{x}_{pp} by virtue of the fact that $Y(\mathbf{x})$ can be generated through sequential simulation with specification of \mathbf{Y}_{pp} (along with specification of \mathbf{Y}_{meas} and the semivariogram models γ_Y). When the log permeability is the only unknown flow parameter considered, the vector of unknowns is defined as $\mathbf{a} = \mathbf{Y}_{\text{pp}}$. In the case where additional flow parameters, such as the values (or log values) of the spatially uniform soil parameters from (3)–(5), then $\mathbf{a} = [\mathbf{Y}_{\text{pp}}, \mathbf{b}]^T$, where $\mathbf{b} = [\log \alpha, \log m, S_w^{\text{res}}, S_w^{\text{sat}}, \dots]^T$. Parameters that could also be included in \mathbf{b} are the parameters of the petrophysical model used to simulate GPR measurements or even parameters of the semivariogram models. Furthermore, the parameters of \mathbf{b} could be considered as heterogeneous, i.e., the method does not require them to be uniform in space. The relationships between \mathbf{a} and observational data can be written as

$$\mathbf{z} = \begin{bmatrix} \mathbf{z}_H \\ \mathbf{z}_{\text{GPR}} \end{bmatrix} = \begin{bmatrix} F_H(\mathbf{a}, \mathbf{Y}_{\text{meas}}) \\ F_{\text{GPR}}(\mathbf{a}, \mathbf{Y}_{\text{meas}}) \end{bmatrix} + \begin{bmatrix} \mathbf{v}_H \\ \mathbf{v}_{\text{GPR}} \end{bmatrix} = F(\mathbf{a}, \mathbf{Y}_{\text{meas}}) + \mathbf{v}, \quad (9)$$

where \mathbf{z} is a vector (of length $M_H \times N_H + M_{\text{GPR}} \times N_{\text{GPR}}$) containing all observational data, F_H is the forward model (non-linear functional) that maps \mathbf{a} and \mathbf{Y}_{meas} to the hydrological measurement domain \mathbf{z}_H , F_{GPR} is the forward model (non-linear functional) that maps \mathbf{a} and \mathbf{Y}_{meas} to the GPR measurement domain \mathbf{z}_{GPR} , F are the combined forward models mapping \mathbf{a} and \mathbf{Y}_{meas} to the

measurement domains, and \mathbf{v} are the measurement errors for \mathbf{z} . Recall that the electrical parameters used in F_{GPR} are a function of the saturation profile, which is itself a function of \mathbf{a} and \mathbf{Y}_{meas} .

The goal of inversion now becomes the estimation of \mathbf{a} given \mathbf{z} . This problem lends itself to the Bayesian, or maximum a posteriori (MAP), framework [34], where we may write the a posteriori probability density function (pdf) of \mathbf{a} given \mathbf{z} as

$$p_{a|z}(\mathbf{a}|\mathbf{z}) = \frac{p_{z|a}(\mathbf{z}|\mathbf{a})p_a(\mathbf{a})}{p_z(\mathbf{z})} = \frac{p_v[\mathbf{z} - F(\mathbf{a})]p_a(\mathbf{a})}{p_z(\mathbf{z})}, \quad (10)$$

where $p_{z|a}$ is the pdf of \mathbf{z} given \mathbf{a} , also referred to as the likelihood function, p_z is the pdf of \mathbf{z} , p_a is the prior pdf of \mathbf{a} , and p_v is the pdf of \mathbf{v} . The second equality in (10) holds only for the case where \mathbf{a} and \mathbf{v} are independent. Prior information traditionally refers to data that is available from sources outside the site of interest, such as measurements collected at nearby sites, or from soil databases [46]. However, in the case of pilot points prior information can also be obtained through interpolation of in situ point measurements, as will be described below.

If p_a and p_v are also assumed to be multi-normal with covariance matrices \mathbf{C}_a and \mathbf{C}_v , respectively, then (10) becomes the multi-normal maximum a posteriori formulation given by

$$p_{a|z}(\mathbf{a}|\mathbf{z}) = c(\mathbf{z}) \exp \left\{ -\frac{1}{2} [\mathbf{z} - F(\mathbf{a})]^T \mathbf{C}_v^{-1} [\mathbf{z} - F(\mathbf{a})] \right\} \cdot \exp \left\{ -\frac{1}{2} [\bar{\mathbf{a}} - \mathbf{a}]^T \mathbf{C}_a^{-1} [\bar{\mathbf{a}} - \mathbf{a}] \right\}, \quad (11)$$

where $\bar{\mathbf{a}}$ is the prior mean of \mathbf{a} , and $c(\mathbf{z})$ is a normalization factor that depends only on \mathbf{z} [34]. We seek not a single value for each parameter, but rather the entire probability distribution for each parameter based on the available measurements. Recall the $Y(\mathbf{x})$ is generated using \mathbf{Y}_{pp} and \mathbf{Y}_{meas} through sequential simulation with random seed numbers. To obtain one realization of the unknown parameters, a single inversion is performed using one seed number. Each inversion consists of minimization of the function given by $-2 \ln p_{a|z}(\mathbf{a}|\mathbf{z})$ with respect to \mathbf{a} . The objective function (OF) for this purpose is given by the following:

$$\text{OF}(\mathbf{a}) = [\mathbf{z} - F(\mathbf{a})]^T \mathbf{C}_v^{-1} [\mathbf{z} - F(\mathbf{a})] + [\bar{\mathbf{a}} - \mathbf{a}]^T \mathbf{C}_a^{-1} [\bar{\mathbf{a}} - \mathbf{a}]. \quad (12)$$

It is worth reiterating that the full MAP solution requires $p_{a|z}(\mathbf{a}|\mathbf{z})$ to be fully formed. Each parameter realization obtained through the minimization of (12) will contribute to $p_{a|z}(\mathbf{a}|\mathbf{z})$. The first term in (12) represents the mismatch between measured and simulated observations, and the second term represents the mismatch between the set of unknown parameters and their prior estimates.

In order to show the separate contributions to the objective function of the pilot points and the additional flow parameters (and only for the case in which the off-diagonals of \mathbf{C}_a are zero) (12) can be written as

$$\text{OF}(\mathbf{a}) = [\mathbf{z} - F(\mathbf{a})]^T \mathbf{C}_v^{-1} [\mathbf{z} - F(\mathbf{a})] + [\bar{\mathbf{Y}}_{\text{pp}} - \mathbf{Y}_{\text{pp}}]^T \times \mathbf{C}_{Y_{\text{pp}}}^{-1} [\bar{\mathbf{Y}}_{\text{pp}} - \mathbf{Y}_{\text{pp}}] + [\bar{\mathbf{b}} - \mathbf{b}]^T \mathbf{C}_b^{-1} [\bar{\mathbf{b}} - \mathbf{b}], \quad (13)$$

where $\bar{\mathbf{Y}}_{\text{pp}}$ and $\bar{\mathbf{b}}$ are the prior means of \mathbf{Y}_{pp} and \mathbf{b} , respectively, and $\mathbf{C}_{Y_{\text{pp}}}$ and \mathbf{C}_b are the corresponding covariance matrices.

While (12) and (13) are of the form of the classic weighted least squares estimator, the approach utilized here is different since these objective functions are being used to calculate of $p_{a|z}(\mathbf{a}|\mathbf{z})$ for the special case of the MAP estimator described above. It should also be said that this framework has the flexibility to handle prior pdfs other than that given in (11). In that case, however, the latter terms in the objective functions of (12) and (13) would take a new form [42], but the procedure would remain unchanged.

Other pilot point implementations have resulted in objective functions for which prior information was commonly implemented through constrained minimization, essentially with an objective function containing the first term of (13) [9,19,32]. The error covariance matrix \mathbf{C}_v was commonly replaced by some relative weighting parameter—though zero measurement error was often assumed. (Recently, the importance of accurately accounting for measurement errors was stressed [23].) McLaughlin and Townley [34] suggested that prior information could be better used through an implementation similar to (13), which happens to be equivalent in form to the MAP estimator we are considering.

In the current approach, values of $\bar{\mathbf{Y}}_{\text{pp}}$ are taken to be the kriging estimates \mathbf{Y}_{krig} , which are derived from point measurements \mathbf{Y}_{meas} [14]. In this way, the minimum variance estimates of \mathbf{Y}_{pp} are obtained with uncertainties quantified through the kriging variance $\sigma_{sk}^2(\mathbf{x})$. Since the diagonal elements of $\mathbf{C}_{Y_{\text{pp}}}$ represent the expected variance of the pilot point parameters, it is then natural to set them equal to the $\sigma_{sk}^2(\mathbf{x})$ estimates. We assume that the off-diagonal elements of $\mathbf{C}_{Y_{\text{pp}}}$ can be approximated as zero (the validity of the assumption that measurement errors are uncorrelated can be verified with the sensitivity analysis procedure presented below). As the prior values $\bar{\mathbf{Y}}_{\text{pp}}$ become less accurate (as $\sigma_{sk}^2(\mathbf{x})$ increases), less weight is assigned to them in the objective function (i.e., the impact of the second term of (13) is lessened). When there are no \mathbf{Y}_{meas} available, the values of $\bar{\mathbf{Y}}_{\text{pp}}$ equal the population mean, and the diagonal values of $\mathbf{C}_{Y_{\text{pp}}}$ equal the population variance.

Estimates of $\bar{\mathbf{b}}$ can represent measurements taken with soil cores at the site of interest. Alternatively, if no such measurements are available, average values may be taken from nearby sites, or from soil parameter data-

bases. In either case, the variance values that populate the covariance matrix \mathbf{C}_b should represent the uncertainty with which the values of $\bar{\mathbf{b}}$ are known.

4.3. Implementation details

We implemented the inversion procedure discussed above in iTOUGH2 [17], a code that provides inverse modeling capabilities to the TOUGH2 flow simulator [39]. In general, inversion proceeds as follows:

1. Observational data (\mathbf{z}) are collected in a field test (or data are simulated for a synthetic study, as is done presently), and their error distributions are quantified.
2. The set of pilot point parameters \mathbf{Y}_{pp} (and locations $\mathbf{x}_{Y_{pp}}$) are defined (2–3 pilot points per correlation length are typically used).
3. An initial log permeability field $Y^0(\mathbf{x})$ is generated with GSLIB [14] using a given seed number. This field is then iteratively modified in steps 5–6.
4. Using the forward models $\mathbf{F}(\mathbf{a})$, which allow for simulation of hydrological and GPR measurements, observational data (\mathbf{z}_{sim}) are simulated and used to calculate the initial value of the objective function (13) for this realization.
5. The values of \mathbf{Y}_{pp} and \mathbf{b} are perturbed via an optimization algorithm (described below), and a new field $Y(\mathbf{x})$ (with the same seed number as that used to generate $Y^0(\mathbf{x})$) is generated using the newly perturbed values. The values of \mathbf{Y}_{pp} are treated as conditioning points in the sequential simulation so that, in essence, the perturbation of a pilot point value is propagated throughout the region near that point, with the extent of perturbation being related to the correlation length.
6. Observational data (\mathbf{z}_{sim}) are simulated with the perturbed field obtained in (5) and used to calculate the new value of the objective function. Steps 5–6 are repeated (until the objective function is minimized). The final estimates of \mathbf{Y}_{pp} and \mathbf{b} for this random field realization are those with minimal deviation from the prior values for which measured and simulated observational data match best.
7. Steps 3–6 are then repeated for the desired number of random field realizations (each with a different seed number).

The estimated log permeability fields (and values of \mathbf{b}) may then be used for predictive hydrological modeling and to generate the a posteriori pdfs of the flow parameters.

In the present work we chose to use the Downhill simplex optimization algorithm. While less efficient than gradient-based methods (e.g., Levenberg–Marquardt), the Downhill Simplex method was chosen since it is robust, its sensitivity to initial conditions is low, and it

requires no assumptions to be made regarding the shape of the objective function, such as it being quadratic or smooth [36,38].

For the synthetic example that follows, inversions were performed for a number of different scenarios using a numerical model with 1200 nodes. Performing 20 inversion realizations typically required 1–2 h of computation time, though this depended on the various parameters (e.g., amount of measurement noise, number of data points) for each scenario. Calculations were done on a PC with a 4-M CPU, 1.80 GHz clock speed, and 512 MB RAM. Though the computational requirements are substantial for this approach, the parallel processing features of iTOUGH2 (not used for obtaining the results presented here) make possible large, 3-D problems of practical relevance.

5. Synthetic example: ponding experiment

A synthetic example involving a ponded infiltration experiment in a two-dimensional vadose zone model (see Fig. 2a) is presented next. The vertical and horizontal

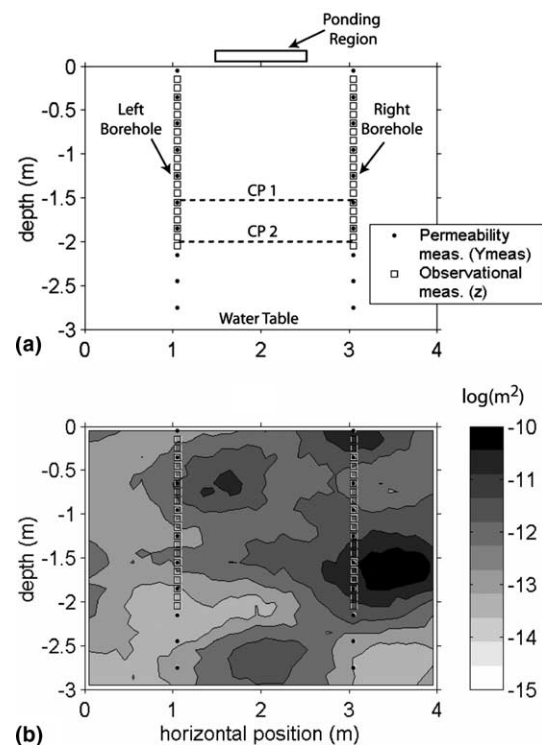


Fig. 2. Synthetic example: ponded infiltration experiment. (a) Experimental geometry and (b) the permeability distribution (unconditional simulation) used in example. Boreholes are located at the horizontal positions of 1 and 3 m. Permeability measurements are taken from each borehole at 30 cm spacing (shown as black dots), water saturation measurements are taken at the boreholes (at open squares), and the pseudo-GPR measurements reflect horizontally averaged water saturation values between the boreholes (between open squares). The control planes used to test inversion performance are shown in (a) and denoted by CP 1 and CP 2.

dimensions for the modeled domain are 3 and 4 m, respectively, and the nodal spacing is 10 cm. The parameters describing the relative permeability and capillary pressure functions of the soil are spatially uniform, as is the soil porosity. Although effects of hysteresis on relative permeability can substantially impact the redistribution of water following infiltration [37], this is not considered in the present work for simplicity. The only non-uniform flow parameter is the permeability, and its log value is modeled as an SRF. In particular, the log permeability field for this model (Fig. 2b) was generated using sequential Gaussian simulation (SGSIM) [14] with a Gaussian anisotropic semivariogram (with variance of 0.5, nugget of 0.01, and effective horizontal and vertical ranges equal to 1.5 and 0.75 m, or integral scales of 0.77 and 0.38 m, respectively). See Table 1 for a summary of the flow parameters used in this example.

The boundary conditions are assumed to be known at all times. While the saturation values are specified along the upper boundary of the model (i.e., the ground surface), their values change during the ponding experiment (described next). The lower boundary of the model is kept fully saturated representing the water table. And the vertical sides of the model are treated as no-flow boundaries.

In order to simulate a single ponded infiltration experiment several steps are required. First, pre-ponding conditions are obtained by simulating gravity-capillary equilibrium; this is done by specifying the water saturation value of 0.3 along the upper boundary of the model (and full saturation along the lower boundary) and then running the flow simulation until steady state is reached. This profile, which is unique for each perme-

ability distribution, is then used as the initial condition for the transient simulation, which is initiated by fully saturating the ponding region (see Fig. 2a). After a simulated duration of ponding of 4 h, the surface is again returned to pre-infiltration conditions (i.e., a saturation value of 0.3 along the entire surface) and the simulation continues for 8 h (making the total simulated ponding time equal to 12 h). Simulated profiles of water saturation are shown in Fig. 3a for several times.

Synthetic measurements were also obtained during the simulated ponded infiltration experiment. (“Synthetic measurements” will subsequently be referred to simply as measurements.) For this purpose, two boreholes that extend from the ground surface to the water table were placed two meters apart (see Fig. 2a). Assumed available from in situ measurements or from laboratory measurements on core samples [16], permeability measurements were taken from each borehole in 30 cm intervals giving 20 point measurements in total (i.e., $M_Y = 20$). Each measurement support volume is equal to that used in the flow modeling.

Borehole water saturation (BHSAT) values were also recorded at 20 depths (up to ~2 m deep with a 10 cm interval) for 35 times in each borehole (i.e., $M_H = 40$ and $N = 35$). These are assumed available through, for example, neutron probe measurements [18]. Measurement error was added to the BHSAT values from a standard normal distribution (zero mean with standard deviation equal to 0.01). In reality, the averaging volume of neutron probe measurements depends on the soil properties surrounding the borehole but this affect is not accounted for here. Fig. 3b shows the BHSAT measurements (before measurement noise is added) for several times in the ponding experiment. Note that lar-

Table 1
Summary of parameters used to construct the (true) model in synthetic example

Description	Parameter values
Flow modeling parameters (Eqs. (1) and (2)) ^a	$\mu_w = 1.002 \times 10^{-3} \text{ Pa s}$ $\rho_w = 1000 \text{ kg/m}^3$, $\phi = 0.3$
Relative permeability and capillary pressure functions (Eqs. (3)–(5)) ^a	$m = 0.4565$, $\alpha = 4.037 \times 10^{-4} \text{ Pa}^{-1}$ $S_w^{\text{res}} = 0.15$ $S_w^{\text{sat}} = 1.0$
Gaussian semivariogram model for log permeability ^b	<i>Horizontal</i> $c_0 = 0.01$, $c_1 = 0.5$ $a = 0.866 \text{ m}$ $r = 1.5 \text{ m}$ ($I = 0.77 \text{ m}$)
↓	<i>Vertical</i> $c_0 = 0.01$, $c_1 = 0.5$ $a = 0.433 \text{ m}$ $r = 0.75 \text{ m}$ ($I = 0.38 \text{ m}$)
$\gamma_Y(h) = c_0 + c_1[1 - \exp(-h^2/a^2)]$	

^a Parameters defined in text.

^b h is separation distance (m), c_0 and c_1 are nugget and variance, respectively; the range and integral scale are measures of spatial persistence given by $r = a\sqrt{3}$, and $I = a\sqrt{\pi}/2$, respectively for the Gaussian semivariogram (for the case where c_0 is small).

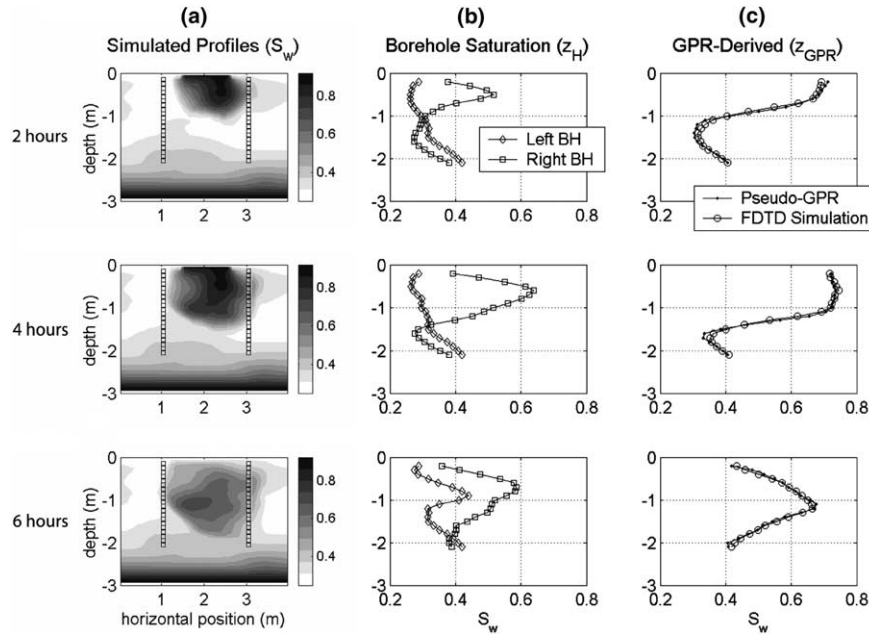


Fig. 3. Simulated profiles of water saturation and the corresponding synthetic measurements (before measurement noise is added) for three separate times during simulated infiltration test. The first column (a) shows the water saturation profiles for 2, 4, and 6 h after the onset of ponding, respectively. Note that the upper portion of the model has begun to dry by 6 h since ponding was applied for only 4 h. The corresponding borehole saturation measurements (BHSAT) for the left and right boreholes are shown in the second column (b). The third column (c) shows for each time a comparison between the water saturation values derived from ZOP measurements simulated with a GPR time domain finite difference (FDTD) code and those obtained by horizontally averaging the simulated water saturation values at each depth (i.e., the pseudo-GPR measurements).

ger increases are observed at the right borehole than at the left due to large scale heterogeneity in permeability (Fig. 3b).

In addition, crosshole GPR (ZOP) measurements are considered in the current example. As discussed earlier, a water saturation profile derived from a ZOP data set represents a depth profile of horizontally averaged inter-borehole water saturation. In previous work, a procedure was described for simulating GPR in variably saturated media [29,30]. In that work, the procedure of Bergmann et al. [3] was followed using an explicit (staggered grid) finite difference time domain (FDTD) algorithm (with 4th and 2nd order accurate approximations for the spatial and time derivatives, respectively). Simulating 250 MHz ZOP surveys with this procedure allows for travel times to be recorded and vertical profiles of water saturation to be obtained using (8) (Fig. 3c). However, similar vertical profiles of water saturation were obtained by calculating the average water saturation in the volume sampled by each GPR antennae pair (also shown in Fig. 3c). This was done by simply taking the arithmetic average of the simulated water saturation values between the boreholes at each measurement depth (with an averaging thickness equal to 10 cm, roughly equal to the vertical resolution of GPR for this frequency). This provided justification for using “pseudo-GPR measurements” in the present study. Namely, horizontally averaged water saturation values are calculated within iTOUGH2 and used as a

proxy for simulated ZOP measurements ($M_{\text{GPR}} = 20$ and $N = 35$). Measurement error was also added to these values (from a standard normal distribution with zero mean and a standard deviation of 0.01).

It should be noted that for shallow measurements the occurrence of refracted waves along the ground surface can make it difficult to identify the direct wave arrival times. For the sake of this synthetic study, we assume that all the GPR measurements are deep enough to allow for the arrival time of the direct waves to be measured. In real world implementation, the region for which meaningful data can be collected depends on GPR antenna frequency and needs to be identified through preliminary surveys.

5.1. Estimating log permeability using different measurement types

At first the analysis is limited to the case in which the log permeability is the only unknown flow parameter (i.e., minimization is performed using (13) with only the first two terms). The benefits of various data sets (i.e., BHSAT, pseudo-GPR, or a combination of both) can be evaluated effectively by comparing models obtained through conditional simulation and inversion with the same seed number (Fig. 4). (Note that a different seed number was used for generating the true model.) As expected, a conditional simulation of the log permeability field (generated with only point measurements of permeability) does

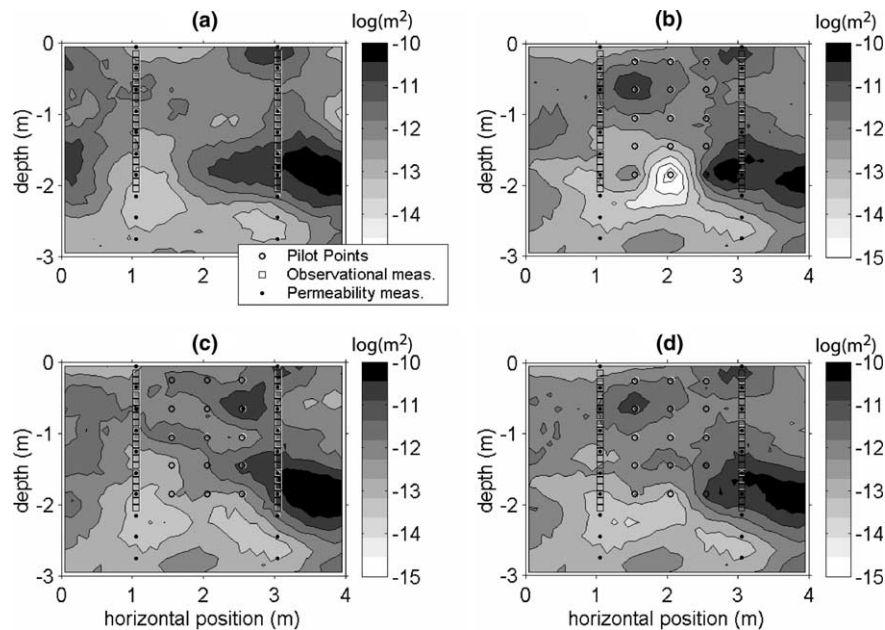


Fig. 4. Log permeability models obtained (a) with conditional simulation, and through inversion using (b) only borehole saturation (BHSAT) measurements, (c) only pseudo-GPR measurements; and (d) pseudo-GPR and BHSAT measurements. The permeability measurement locations (Y_{meas}) used as conditioning points are shown with black dots, the observational data (z) locations are shown with squares, and the pilot point (Y_{pp}) locations are shown with open circles.

not capture the main features of the true model (Fig. 2b) except near the point measurement locations (Fig. 4a). An unsatisfactory model (with an anomalous low permeability zone) is also obtained through inversion of BHSAT measurements alone (Fig. 4b).

Including the easily collected GPR measurements in inversion allows for improved models of log permeability to be obtained. Inversion with only the pseudo-GPR measurements results in a model (Fig. 4c) with features that are similar to the true model but are not placed in the correct lateral positions (e.g., the high permeability zone in the upper half of the model). This occurrence is explained by the fact that while ZOP measurements reflect average values of water saturation between boreholes, they are insensitive to lateral variations in water saturation (and thus in permeability). On the other hand, the combined use of the pseudo-GPR with additional local measurements (i.e., BHSAT measurements) results in a model that appears quite similar to the true model (Fig. 4d).

It should be noted that in each case shown in Fig. 4, significant deviation from the true model is seen in locations where no data were collected and no pilot points were placed (outside the inter-borehole region and toward the bottom of the model).

The observational data (z) available for inversion in this example are depicted in Fig. 5. For the model generated by conditional simulation (i.e., without inversion), the mismatch between measured and simulated observations is substantial (Fig. 5a). Whereas, inversion of the pseudo-GPR and BHSAT measure-

ments (as performed to obtain the model in Fig. 4d) allows for a good match between the measured and simulated observations (Fig. 5b).

While the models discussed above are based on one random field realization (i.e., one seed number), inversions on 20 different realizations were performed in total, giving estimates of the mean and standard deviation surfaces (Fig. 6). Note that for the case of conditional simulation, the high permeability zone seen in the inter-borehole region of the true model is not predicted and that away from the permeability measurements the standard deviation values are high (Fig. 6a). The large scale patterns of the true model are better reflected in the mean surface for the models obtained using only pseudo-GPR measurements (Fig. 6b), and for the models obtained using both pseudo-GPR and BHSAT measurements (Fig. 6c). To facilitate comparison, Fig. 7 shows a vertical slice of the true model with vertical slices from the estimated mean fields (from Fig. 6). Note that for both cases involving inversion (Fig. 7b–c), the mean fields match well, at least for depths above -2 m. The lowest prediction error results with the combined use of pseudo-GPR and BHSAT measurements (Fig. 7b–c).

As discussed earlier, a benefit of the inversion methodology lies in its ability to generate models with specified semivariograms. The true log permeability model used in this example was taken as an unconditional realization generated with the theoretical semivariograms shown in Fig. 8 (also see Table 1). While the mean (horizontal and vertical) semivariograms for 20 unconditional realizations match the theoretical semivario-

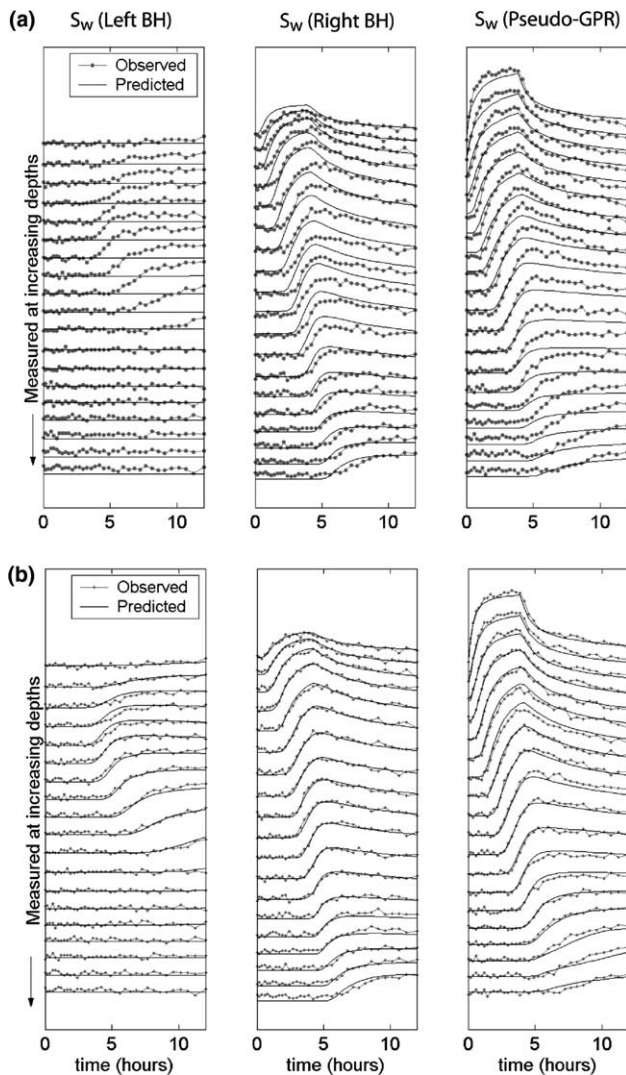


Fig. 5. Comparison of measured observations (dots) and predicted/simulated observations (lines) for permeability models obtained through (a) conditional simulation, and (b) inversion. Observational data (z) include borehole water saturation measurements (left and middle columns), and water saturation inferred from pseudo-GPR measurements (right column).

grams reasonably well, those for the true model vary somewhat from the theoretical model (especially beyond separation distances of 1 m, or 1.3 integral scales, in the horizontal direction). However, inversion of pseudo-GPR and BHSAT measurements gives models whose mean semivariograms, in fact, match the true model better (Fig. 8).

5.2. Predicting breakthrough curves

Ultimately, site characterization requires models that allow for prediction of relevant fluid flow phenomena. While there are many measures one could examine to assess the performance of calibrated models, the phe-

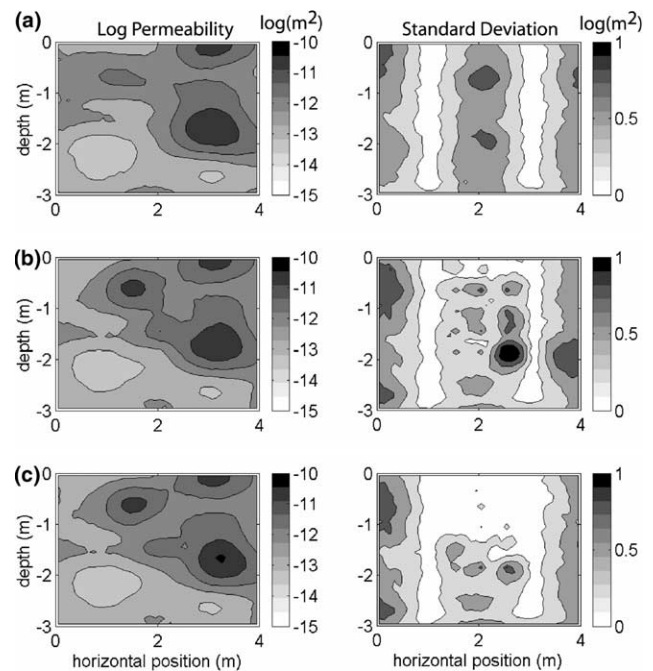


Fig. 6. Mean and standard deviation surfaces (left and right columns, respectively) of 20 realizations for three cases: (a) conditional simulations, (b) inversion using only pseudo-GPR, and (c) inversion using BHSAT and pseudo-GPR.

nomenon of interest depends on the particular application. We chose to evaluate the ability of the calibrated models to predict the breakthrough of water caused by the ponding experiment. Accordingly, the true breakthrough curves (BTC) at several control planes (as depicted in Fig. 2a) are compared with predicted BTCs in Fig. 9. (The BTC is defined as the time-varying total flow rate across a control plane.) For this case, conditional realizations fail to accurately predict breakthrough (Fig. 9a). Performing inversion with BHSAT measurements improves the prediction significantly by allowing for better prediction of the initial breakthrough times, though the absolute values remain inaccurate (Fig. 9b). Dramatic improvements in prediction are obtained through inversion with pseudo-GPR measurements (using only pseudo-GPR or using the combination of pseudo-GPR and BHSAT measurements) (Fig. 9c and d). Predictions at the lower control plane are for the most part more scattered than at the upper control plane in part because the region sampled by the hydrological and GPR measurements only reaches a depth of about -2 m. The observational data are not sensitive to modification of the permeability fields at or below this depth.

Prediction of breakthrough over entire control planes was equally good when GPR measurements were used alone or together with BHSAT measurements. However, for reasons discussed above, it was found that the combination of both GPR and BHSAT observations is required in order to obtain accurate lateral variations in

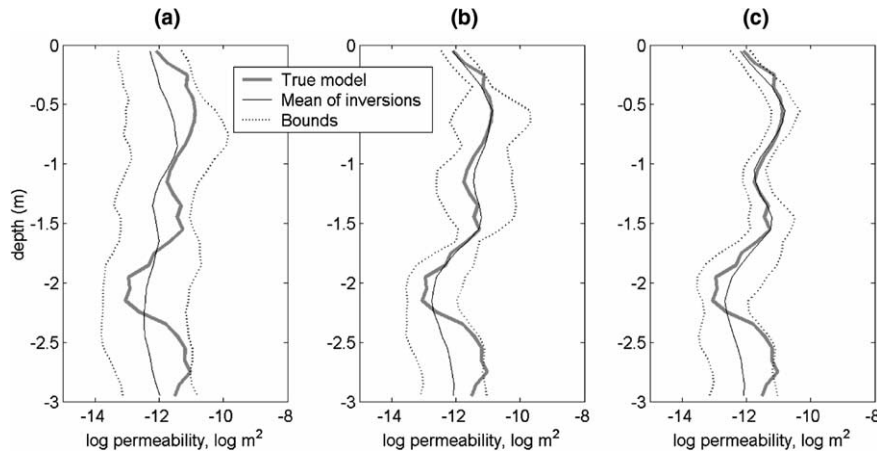


Fig. 7. Vertical cross-section (at arbitrary horizontal position of 1.85 m) of true log permeability model (gray) and mean surfaces obtained from 20 inversion realizations (black lines) for (a) conditional simulation, (b) inversion using only pseudo-GPR, and (c) inversion using BHSAT and pseudo-GPR. The estimation bounds (the mean surface ± 2 times the standard deviations) are shown with dotted lines.

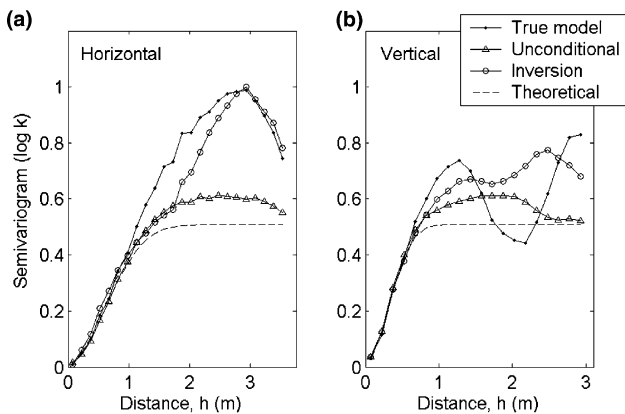


Fig. 8. The horizontal (left) and vertical (right) log permeability semivariograms for: the unconditional realization that is used as the true model (dotted line); the mean of 20 unconditionally generated fields (triangles); the mean of 20 fields obtained through inversion with BHSAT and pseudo-GPR measurements (circles), and; the theoretical model.

the predicted BTCs (Fig. 10). Prediction over a support volume smaller than what is measured with the ZOP surveys requires more data and a better representation of local conditions, that is, point measurements of saturation at the boreholes in this case.

5.3. Considerations with an additional flow parameter

Previously, we assumed that the flow parameters of the capillary pressure and relative permeability functions were known (i.e., experimentally determined) and error free. In this section, the following issues are considered: how sensitive are inversions to error in a measured (and assumed known) flow parameter (specifically, α of Eq. (4)); and, can its value be estimated jointly with the permeability distribution? In the previous sections,

the amount of data available for inversion was large and rather idealized (observational data were collected at 36 times, making $N = 36$, within 12 h). In this section, a somewhat less ideal, but more practical scenario is considered—observations at only 12 times ($N = 12$) within the same time frame are assumed available for inversion. The two cases considered are briefly described next before discussing the results:

Case 1: Estimating $\log k$ with error in α

Here we consider the possibility that the parameter α has been measured inaccurately (or an incorrect value has been assumed) and examine the impact that this error has on inversion and subsequent BTC predictions. Without acknowledging or accounting for this error, inversions are performed as before: the permeability distribution is estimated through inversion (with pseudo-GPR and BHSAT), and BTC predictions are made. While α is assumed to be uniform, its “measured” (log) value is given an error of 6%, and the remaining flow parameter values remain error free (Tables 1 and 2). The resulting capillary pressure function (4) used in the forward model to simulate z is no longer correct (not shown). Note that only a small amount of error is considered so that we may evaluate if even a small deviation from the true value affects the inversion results significantly.

Case 2: Estimating $\log \alpha$ together with $\log k$

Until now, the log permeability was the only parameter considered unknown and the value of α was fixed during inversion. In this case, the permeability distribution and the log value of α are estimated through minimization of (13) with all three terms. Now, $\mathbf{b} = [\alpha]$, and the prior value $\bar{\mathbf{b}}$ is taken as that which was experimentally determined (e.g., from core measurements) or taken from values measured at nearby sites, or from an appropriate soil database. Estimates of the expected

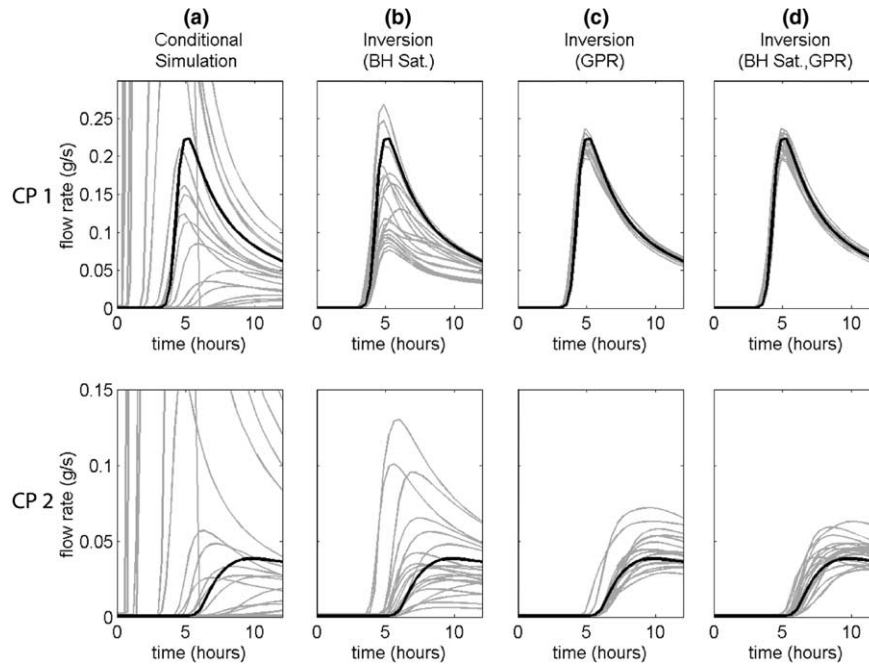


Fig. 9. Breakthrough curves (total flow rates in g/s) at two control planes CP 1 and CP 2 (as depicted in Fig. 2a) for several cases: (a) conditional simulation; (b) inversion with BHSAT; (c) inversion with only pseudo-GPR; and (d) inversion with pseudo-GPR and BHSAT. The true BTC is shown in black, and predictions from 20 inversions (obtained using different seed numbers) are shown with gray lines.

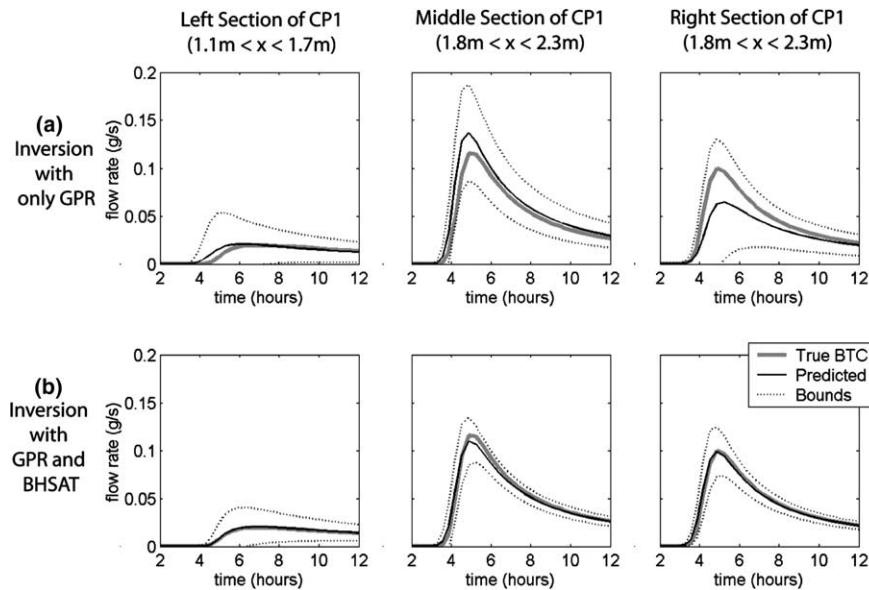


Fig. 10. Lateral variations in BTCs predicted at upper control plane (CP 1) using models obtained through inversion with (a) pseudo-GPR alone, and (b) pseudo-GPR and BHSAT. The flow rate in the left, middle and right sections from each control plane are shown in the left, middle, and right columns, respectively. BTCs for the true model are shown with thick gray lines, while the predicted BTCs (mean from 20 inversions) are shown with black lines, and the prediction bounds (the mean surface ± 2 times the standard deviations) are shown with dotted lines.

variance for this parameter comprise the diagonal matrix C_b . After performing inversions using the same observational data as in the first case, multiple estimates of α and the permeability field are obtained.

Assuming an inaccurate value of α for inversion (Case 1) is seen to affect BTC prediction dramatically—the predicted mean is inaccurate and the uncertainty bounds

are large (Fig. 11a). When, on the other hand, α was estimated together with the log permeability (Case 2), the corresponding mean BTC shows an improved prediction with decreased uncertainty bounds (Fig. 11b). Similar conclusions are drawn in terms of parameter estimation and uncertainty, as depicted in Fig. 12. These results suggest that a prudent way to account for

Table 2

Assigned/estimated parameters for various scenarios involving α^*

	$\log \alpha$			σ_z	N
	Assigned	Estimated (% error)	Standard deviation		
True model	-3.394	—	—	—	—
Error in α (Figs. 11a and 12a)	-3.600	—	—	0.01	12
Estimation of $\log \alpha$ (Figs. 11b, 12b, and 13a)	—	-3.406 (0.37)	0.034	0.01	12
Decreased N (Fig. 13a)	—	-3.401 (0.23)	0.039	0.01	6
Increased σ_z (Fig. 13b)	—	-3.41 (0.49)	0.030	0.10	12
Decreased N , Increased σ_z (Fig. 13b)	—	-3.367 (0.80)	0.037	0.10	6

* Units of $\log \alpha$ are $\log (\text{Pa}^{-1})$, remaining parameters are dimensionless. σ_z is the standard deviation of the (zero mean) noise added to the observational measurements z . For each case, $M_Y = 20$, $M_{\text{GPR}} = 20$, $M_H = 40$.

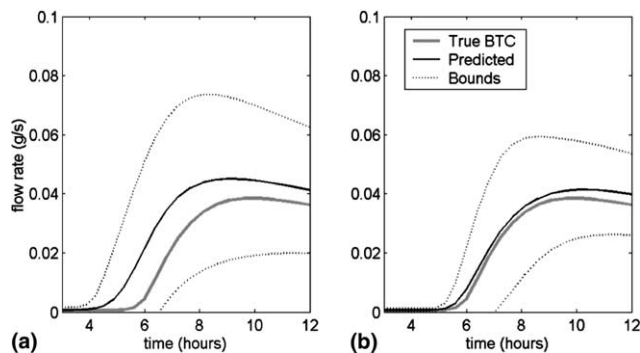


Fig. 11. Considerations with flow parameter α . Inversions for permeability were performed with a slightly inaccurate value of α to give the BTC (at CP 2) shown in (a). The BTC shown in (b) is predicted when values of $\log \alpha$ are estimated jointly with the permeability distribution. For each case, the true BTC is shown with a thick gray line, and the predicted BTC (mean of 20 realizations) is shown with a black line, and the prediction bounds (the mean surface ± 2 times the standard deviations) are shown with dotted lines.

uncertainty in measured (or assumed) values of α , or other flow parameters, is through their estimation together with the log permeability distribution.

5.4. Sensitivity to sampling frequency and measurement error

The sensitivity of inversion results to temporal sampling and measurement error was also examined. With a decrease in the number of times at which observational data were collected (from $N = 12$ to 6) within the 12 h experiment, a slight increase in deviation from the true BTC was observed, though the initial breakthrough time was still close to that for the true model (Fig. 13a). However, when the standard deviation of the measurement error is increased by a factor of 10 (from $\sigma_z = 0.01$ to 0.1), reducing the number of observational data has a more substantial effect (Fig. 13b). In fact, the prediction bounds for the cases with increased measurement error

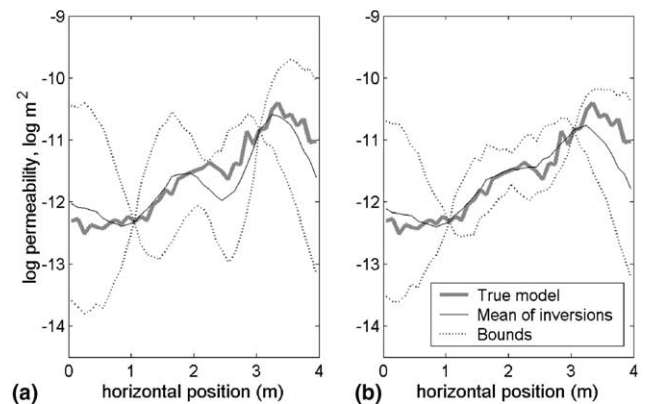


Fig. 12. Horizontal cross-section (at depth of -1.25 m) of true log permeability model (gray) and mean surfaces obtained from 20 realizations (black lines) for (a) inversion using incorrect α and (b) inversions in which both log permeability and α are estimated. The estimation bounds (the mean surface ± 2 times the estimated standard deviations) are shown with dotted lines. Note that the conditioning data points are at horizontal positions of 1 and 3 m. See Table 2.

fail to envelop the true BTC. The impact of increased measurement error and decreased number of observational data on estimation of the flow parameter α is minor (Table 2).

5.5. Experimental design considerations

In designing the present experiment, considerations should include identification of optimal ponding conditions (e.g., lateral placement and duration of the ponding source) and measurement strategies (e.g., data types, locations, and temporal sampling strategies). Alternate design scenarios can be investigated without needing to perform flow inversions through sensitivity analyses [34]. For non-linear problems that are approximately linear near the solution (and for data

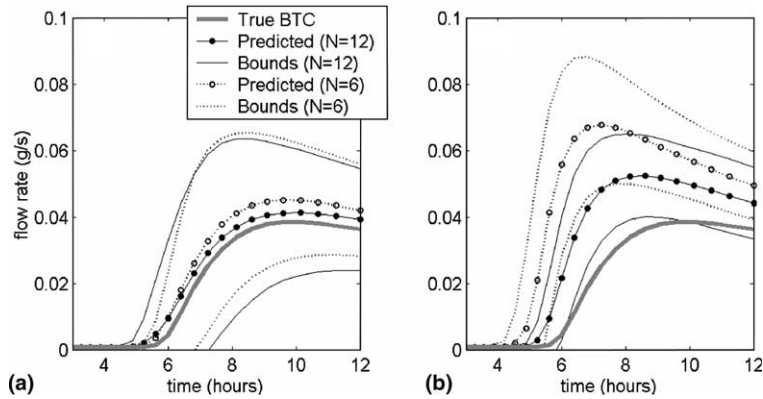


Fig. 13. BTC predictions at CP 2 for models obtained through inversion with decreasing temporal sampling interval (i.e., decreasing N) and increasing measurement errors (σ_z). Two cases of measurement error were considered: (a) $\sigma_z = 0.01$ and (b) $\sigma_z = 0.10$. For both cases, the true BTC is shown with a thick gray line, and the predicted BTCs for $N = 12$ and 6 are shown with solid and open circles, respectively. The bounds (the mean surface ± 2 times the estimated standard deviations) for these respective cases are shown with thin solid lines and dotted lines. Also see Table 2.

with normally distributed measurement errors), the parameter covariance matrix is estimated through

$$\mathbf{C}_a = (\mathbf{J}^T \mathbf{C}_v^{-1} \mathbf{J})^{-1}, \quad (14)$$

where the sensitivity coefficient J_{ij} , a measure of the sensitivity of the observational data z_i to changes in parameters a_j , is given by

$$J_{ij} = \frac{\partial z_i}{\partial a_j}, \quad (15)$$

which is calculated numerically using the perturbation method. It follows that resulting estimates of parameter variance σ_a^2 (contained in the diagonal terms of \mathbf{C}_a) are inversely proportional to the size of the sensitivity coefficients. Competing experimental designs can be evaluated before collecting data by estimating parameter variance in this way for a hypothetical model.

This method was used to investigate the sensitivity of parameter uncertainty to time periods for which observational data are collected. Estimated uncertainty in the pilot point parameters is depicted in Fig. 14 for various cases. The lowest parameter uncertainties are achieved by using all data points, and similarly low values are achieved using only early-time data. However, parameter uncertainty is increased considerably when only late-time data were used. From these observations it can be concluded that the sharp fronts of water saturation seen in the early time data (Fig. 5) are more sensitive to the parameters than are the gradual variations seen in the late time data. Also note the high degree of uncertainty that results with inversion of only (pre-ponding) steady state data points.

The duration of ponding was also investigated. While increasing ponding time from 1 h initially decreased the expected parameter uncertainty, only modest decreases in uncertainty were gained by extending the ponding duration beyond 4 h (not shown). In addition, the ex-

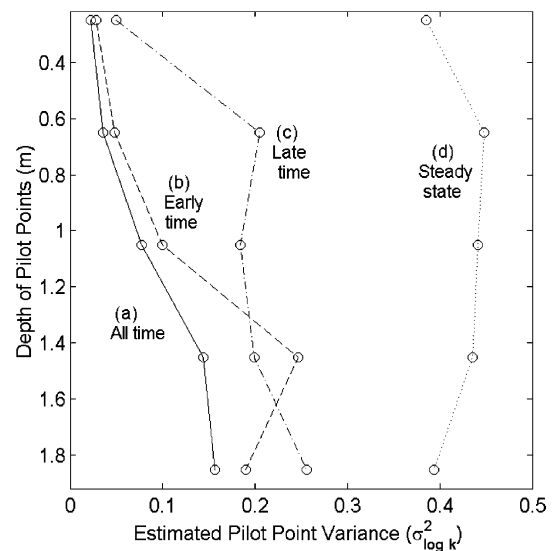


Fig. 14. Estimated variance for the pilot points located along the center line of the model (at a horizontal position of 2 m in Fig. 2). Estimates were obtained by extracting diagonal terms from the \mathbf{C}_a matrix, calculated through Equation (14) in iTOUGH2, for various cases of observational data: (a) all time (12 observations between 0 and 12 h after ponding); (b) early time (8 observations between 0 and 5.5 h); (c) late time (4 observations between 6.8 and 12 h), and; (d) only steady state data (one observation before onset of ponding).

pected parameter uncertainty varied with lateral placement of the ponding source on the surface, with the lowest overall value resulting from placement in the center of the model (also not shown).

6. Summary and conclusions

A method that allows transient hydrological and geophysical measurements to be used for estimating permeability distributions and other flow parameters in the vadose zone was described. The MAP method

provided a framework within which concepts from the pilot point method could be incorporated. Application of a pilot point procedure allows for the generation of multiple parameter distributions that reproduce point measurements, contain the specified patterns of spatial correlation, and are consistent with measured hydrological and geophysical data. The obtained parameter distributions can be used for hydrological modeling. A posteriori parameter pdfs are also obtained and allow for quantification of parameter uncertainty.

A synthetic example indicated that inversion with different data types, including transient hydrological and GPR measurements, allows for good prediction of flow phenomena. While GPR measurements offer the benefit of non-intrusively monitoring changes in water saturation over large distances, measurements collected in the ZOP configuration are insensitive to lateral variations in flow. To predict BTCs with accurate lateral variations, the joint use of ZOP measurements with additional local measurements (BHSAT) was necessary. In any case, prediction of breakthrough was poorest in regions without pilot points or observational data.

While slight error in a measured parameter of the capillary pressure function (α) caused a decrease in accuracy (and increase in uncertainty) in estimation of the permeability field and subsequent flow prediction, it was found that error in the measured log value of α could be accommodated if this parameter was allowed to vary during inversion (i.e., if it is jointly estimated with log permeability). Also, the sensitivity of results to increasing error in observational data and decreasing number of observational data was investigated.

A method for evaluating experimental designs was used to help identify optimal ponding conditions and temporal sampling strategies without needing to perform flow inversions. Observations of particular relevance were that transient data decrease estimation uncertainty compared to steady state data, and that early-time data are seen to decrease estimation uncertainty more than late-time data.

A limitation of the current implementation, but not in the approach itself, lies in the assumption that the log permeability is the only non-uniform parameter since in reality additional flow parameters are commonly non-uniform and possibly correlated with each other. The sensitivity of the model predictions to variations in the flow parameters other than the permeability should be considered. Additionally, it was assumed that spatial correlation patterns of log permeability are known, though this is not always the case. An improved implementation of the approach, which could be done relatively easily, would include estimation of the semivariogram parameters. In this case, a semivariogram model would be chosen (e.g., Gaussian or Exponential), and as its parameters (e.g., range and variance) were perturbed through sequential simulation, the weight of

the prior values would change depending on the perturbed semivariogram model. Also, we have thus far assumed that pre-infiltration conditions are at steady state, which in reality is not always the case, and we have assumed that the boundary conditions are known. Evaluating the impact of uncertainty in boundary conditions and initial conditions on model prediction is also left for future research.

Future investigations will be performed using a more sophisticated forward model of GPR that allows for the simulation of travel times within iTOUGH2 using arbitrary antennae configurations in 3-D models.

Acknowledgements

This work was supported by the US Department of Agriculture NRI grant 2001-35102-09866 Ground-Penetrating Radar: Development of a Vineyard Management Tool, and by US Department of Energy under Contract No. DE-AC03-76SF00098. The authors would like to thank the anonymous reviewers for their constructive feedback and suggestions.

References

- [1] Alumbaugh D, Chang PY, Paprocki L, Brainard JR, Glass RJ, Rautman CA. Estimating moisture contents in the vadose zone using cross-borehole ground penetrating radar: a study of accuracy and repeatability. *Water Resour Res* 2002;38(12):1309.
- [2] Bear J. Dynamics of fluids in porous media. New York: Dover Publications, Inc.; 1988.
- [3] Bergmann T, Robertsson JOA, Holliger K. Finite-difference modeling of electromagnetic wave propagation in dispersive and attenuating media. *Geophysics* 1998;63(3):856–67.
- [4] Binley A, Cassiani G, Middleton R, Winship P. Vadose zone flow model parameterization using cross-borehole radar and resistivity imaging. *J Hydrol* 2002;267:147–59.
- [5] Binley A, Winship P, Middleton R, Pokar M, West J. High-resolution characterization of vadose zone dynamics using cross-borehole radar. *Water Resour Res* 2001;37(11):2639–52.
- [6] Cai J, McMechan GA. Ray-based synthesis of bistatic ground penetrating radar profiles. *Geophysics* 1995;60:87–96.
- [7] Carrera J, Neuman SP. Estimation of aquifer parameters under transient and steady state conditions. 2: Uniqueness, stability, and solution algorithms. *Water Resour Res* 1986;22:211–27.
- [8] Casper DA, Kung K-JS. Simulation of ground-penetrating radar waves in a 2-D soil model. *Geophysics* 1996;61:1034–49.
- [9] Certes C, de Marsily G. Application of the pilot point method to the identification of aquifer transmissivities. *Adv Water Resour* 1991;14(5):284–300.
- [10] Cooley RL. An analysis of the pilot point methodology for automated calibration of an ensemble of conditionally simulated transmissivity fields. *Water Resour Res* 2000;36(4):1159–64.
- [11] Dane JH, Hruska S. In situ determination of soil hydraulic properties during drainage. *Soil Sci Soc Am J* 1983;47:619–24.
- [12] Daniels DJ. Surface penetrating radar. London: Institute of Electrical Engineers; 1996.
- [13] Davis JL, Annan AP. Ground-penetrating radar for high-resolution mapping of soil and rock stratigraphy. *Geophys Prospect* 1989;37:531–51.

- [14] Deutsch CV, Journel AG. *GSLIB: geostatistical software library and user's guide*. New York: Oxford University Press; 1992.
- [15] Eppstein MJ, Dougherty DE. Efficient three-dimensional data inversion: soil characterization and moisture monitoring from cross-well ground-penetrating radar at a Vermont test site. *Water Resour Res* 1998;34(8):1889–900.
- [16] Faybishenko B. Vadose zone characterization and monitoring: current technologies, applications, and future developments. In: Looney BB, Falta RW, editors. *Vadose zone: science and technology solutions*. Ohio: Battelle Press; 2000. p. 133–509.
- [17] Finsterle S. *iTOUGH2 User's Guide*. Report LBNL-40040. Lawrence Berkeley National Laboratory, Berkeley, CA, 1999.
- [18] Gardner WH. Water content, in methods of soil analysis. Part 1. Physical and mineralogical methods—agronomy monograph 9, 2nd ed. American Society of Agronomy—Soil Science Society of America, Madison, Wisconsin: 1986. p. 493–544.
- [19] Gomez-Hernandez JJ, Sahuquillo A, Capilla JE. Stochastic simulation of transmissivity fields conditional to both transmissivity and piezometric data. 1. Theory. *J Hydrol* 1997;203:162–74.
- [20] Gomez-Hernandez JJ, Srivastava RM. ISIM3D: an ANSI-C three-dimensional multiple indicator conditional simulation program. *Comput Geosci* 1990;16(4):395–440.
- [21] Greaves RJ, Lesmes DP, Lee JM, Toksoz MN. Velocity variations and water content estimated from multi-offset, ground-penetrating radar. *Geophysics* 1996;61(3):683–95.
- [22] Grote K, Hubbard S, Rubin Y. Field-scale estimation of volumetric water content using ground-penetrating radar ground wave techniques. *Water Resour Res* 2003;39(11):1321.
- [23] Hendricks Franssen HJWM, Gomez-Hernandez JJ. Impact of measurement errors in stochastic inverse conditional modelling by the self-calibrating approach. *Adv Water Resour* 2003;26:501–11.
- [24] Hollenbeck KJ, Jensen KH. Maximum-likelihood estimation of unsaturated hydraulic parameters. *J Hydrol* 1998;210:192–205.
- [25] Hubbard SS, Rubin Y, Majer E. Ground-penetrating-radar-assisted saturation and permeability estimation in bimodal systems. *Water Resour Res* 1997;33(5):971–90.
- [26] Huisman JA, Hubbard SS, Redman JD, Annan AP. Measuring soil water content with ground penetrating radar: a review. *Vadose Zone J* 2003;2:476–91.
- [27] Jury WA, Russo D, Sposito G, Elabd H. The spatial variability of water and solute transport properties in unsaturated soil: I. Analysis of property variation and spatial structure with statistical models. *Hilgardia* 1987;55:1–32.
- [28] Kool JB, Parker JC, van Genuchten MT. Determining soil hydraulic properties from one-step outflow experiments by parameter estimation. I. Theory and numerical studies. *Soil Sci Soc Am J* 1985;49:1348–54.
- [29] Kowalsky MB, Dietrich P, Teutsch G, Rubin Y. Forward modeling of ground-penetrating radar data using digitized outcrop images and multiple scenarios of water saturation. *Water Resour Res* 2001;37(6):1615–25.
- [30] Kowalsky MB, Rubin Y, Dietrich P. The use of ground-penetrating radar for characterizing sediments under transient flow. In: Bridge J, Hyndman D, editors. *Aquifer characterization*, in press.
- [31] Kunz KS, Luebbers RJ. *The finite difference time domain method for electromagnetics*. Boca Raton: CRC Press; 1993.
- [32] LaVenue AM, Pickens JF. Application of a coupled adjoint sensitivity and kriging approach to calibrate a groundwater flow model. *Water Resour Res* 1992;28(6):1543–70.
- [33] de Marsily G. Spatial variability of properties in porous media: a stochastic approach. In: Bear J, Corapcioglu MY, editors. *Fundamentals of transport in porous media*. Boston: Martinus Nijhoff; 1994. p. 719–69.
- [34] McLaughlin D, Townley LR. A reassessment of the groundwater inverse problem. *Water Resour Res* 1996;32(5):1131–61.
- [35] Mishra S, Parker JC. Parameter estimation for coupled unsaturated flow and transport. *Water Resour Res* 1989;25(3):385–96.
- [36] Nelder JA, Mead R. A simplex method for function minimization. *Comput J* 1965;7:308–13.
- [37] Philip JR. Horizontal redistribution with capillary hysteresis. *Water Resour Res* 1991;27(7):1459–69.
- [38] Press WH, Teukolsky SA, Vetterling WT, Flannery BP, editors. *Numerical recipes in Fortran*. 2nd edition. New York: Cambridge Univ. Press; 1992.
- [39] Pruess K, Oldenburg C, Moridis G. *TOUGH2 User's Guide, Version 2.0*, Report LBNL-43134, Lawrence Berkeley National Laboratory, Berkeley, California, 1999.
- [40] RamaRao BS, de Marsily G, Marietta MG. Pilot point methodology for automated calibration of an ensemble of conditionally simulated transmissivity fields. I: Theory and computational experiments. *Water Resour Res* 1995;31(3):475–93.
- [41] Roth KR, Schulin R, Fluhler H, Attinger W. Calibration of time domain reflectometry for water content measurement using a composite dielectric approach. *Water Resour Res* 1990;26:2267–73.
- [42] Rubin Y. *Applied stochastic hydrogeology*. New York: Oxford University Press; 2003.
- [43] Rubin Y, Bellin A. Conditional simulation of geologic media with evolving scales of heterogeneity. In: Sposito G, editor. *Scale dependence and scale invariance*. Cambridge University Press; 1998.
- [44] Russo D, Bouton M. Statistical analysis of spatial variability in unsaturated flow parameters. *Water Resour Res* 1992;28:1911–25.
- [45] Russo D, Bresler E, Shani U, Parker JC. Analyses of infiltration events in relation to determining soil hydraulic properties by inverse problem methodology. *Water Resour Res* 1991;27(6):1361–73.
- [46] Schaap MG, Leij FJ. Database related accuracy and uncertainty of pedotransfer functions. *Soil Sci* 1998;163:765–79.
- [47] Simunek J, van Genuchten MT. Estimating soil hydraulic properties from tension disc infiltrometer data by numerical inversion. *Water Resour Res* 1996;32(9):2683–96.
- [48] Topp GC, Davis JL, Annan AP. Electromagnetic determination of soil water content: measurements in coaxial transmission lines. *Water Resour Res* 1980;16(3):574–82.
- [49] Turner G, Siggins AF. Constant Q attenuation of subsurface radar pulses. *Geophysics* 1994;59(8):1192–200.
- [50] van Genuchten MT. A closed-form equation for predicting the hydraulic conductivity of unsaturated soils. *Soil Sci Soc Am J* 1980;44:892–8.
- [51] van Overmeeren RA, Sariowan SV, Gehrels JC. Ground penetrating radar for determining volumetric soil water content; results of comparative measurements at two test sites. *J Hydrology* 1997;197:316–38.
- [52] Wen X-H, Deutsch CV, Cullick AS. Construction of geostatistical aquifer models integrating dynamic flow and tracer data using inverse technique. *J Hydrol* 2002;255:151–68.
- [53] Yeh T-C, Liu S, Glass RJ, Baker K, Brainard JR, Alumbaugh D, LaBrecque D. A geostatistically based inverse model for electrical resistivity surveys and its applications to vadose zone hydrology. *Water Resour Res* 2002;38(12):1278.
- [54] Zhou Z-Y, Young MH, Li Z, Wierenga PJ. Estimation of depth averaged unsaturated soil hydraulic properties from infiltration experiments. *J Hydrol* 2001;242:26–42.